Saharan dust intrusions over the northern Mediterranean region in the frame of EARLINET (2014-2017): Properties and impact in radiative forcing

Ourania Soupiona[1], Alexandros Papayannis[1], Panagiotis Kokkalis[2], Romanos Foskinis[1], Guadalupe Sánchez Hernández[3,4], Pablo Ortiz-Amezcua[3,4], Maria Mylonaki[1], Christina-Anna Papanikolaou[1], Nikolaos Papagiannopoulos[5], Stefanos Samaras[6], Silke Groß[7], Rodanthi-Elisavet Mamouri[8,9], Lucas Alados-Arboledas[3,4], Aldo Amodeo[5], Basil Psiloglou[10]

[1]School of Applied Mathematics and Physical Sciences, Dept. of Physics, National Technical University of Athens, 15780, Greece
[2]Department of Physics, Kuwait University, Safat, 13060, Kuwait.
[3]Department of Applied Physics, University of Granada, Granada,18071, Spain
[4]Andalusian Institute for Earth System Research, Granada, 18006, Spain
[5]Consiglio Nazionale delle Ricerche, Istituto di Metodologie per l'AnalisiAmbientale, Tito Scalo, 85050, Italy
[6]German Aerospace Center (DLR), German Remote Sensing Datacenter (DFD), Wessling, Germany
[7]Institute of Atmospheric Physics, DeutschesZentrumfürLuft- und Raumfahrt (DLR), Oberpfaffenhofen, 82234, Germany
[8]Cyprus University of Technology, Dep. of Civil Engineering and Geomatics, Limassol, Cyprus
[9]ERATOSTHENES Centre of Excellence, Limassol, Cyprus
[10]nstitute for Environmental Research and Sustainable Development, National Observatory of Athens, Palaia Penteli, Athens, Greece

* Correspondence to: Ourania Soupiona (raniaphd@mail.ntua.gr)

Abstract

Remote sensing measurements of aerosols using depolarization Raman Lidar systems from 4 EARLINET (European Aerosol research Lidar Network) stations are used for a comprehensive analysis of Saharan dust events over the Mediterranean basin in the period 2014-2017. In this period, we selected to study 51 dust events regarding the geometrical, optical and microphysical properties of dust particles, classifying them and assessing their radiative forcing effect on the atmosphere. From West to East, the stations of Granada, Potenza, Athens and Limassol were selected as representative Mediterranean cities regularly affected by Saharan dust intrusions. Emphasis was given on lidar measurements in the visible (532 nm) and specifically on the consistency of the particle linear depolarization ratio (δ_{p532}), the extinction-to-backscatter lidar ratio (LR_{532}) and the Aerosol Optical Thickness (AOT_{532}) within the observed dust layers. We found mean δ_{p532} values of 0.24±0.05, 0.26±0.06, 0.28±0.05 and 0.28±0.04, mean LR_{532} values of 52±8 sr, 51±9 sr, 52±9 sr and 49±6 sr, and mean AOT_{532} values of 0.40±0.31, 0.11±0.07, 0.12±0.10 and 0.32±0.17, for Granada, Potenza, Athens and Limassol, respectively. The mean layer thickness values were found to range from ~1700 to ~3400 m. Additionally, based also on a previous aerosol type classification scheme provided by airborne High Spectral Resolution Lidar (HSRL) observations and on air mass backward trajectory analysis, a clustering analysis was performed in order to identify the major mixing aerosol types over the studied area. Furthermore, a synergy of lidar measurements and modeling was used to deeply analyze the solar and thermal radiative forcing of airborne dust. In total, a cooling behavior in the solar range and a significantly lower heating behavior in the thermal range was estimated. Depending on the dust optical and geometrical properties, the load intensity and the solar zenith angle (SZA), the estimated solar radiative forcing values range from -59 to -22 W m^{-2} at the surface and from -24 to -1 W m^{-2} at the top of the atmosphere (TOA). Similarly, in the thermal spectral range these values range from +2 to +4 W m^{-2} for the surface and from +1 to +3 W m^{-2} for the TOA. Finally, the radiative forcing seems to be inversely proportional to the dust mixing ratio, since higher absolute values are estimated for less mixed dust layers.

1. Introduction

The Saharan desert is one of the major dust sources globally, with dust advections to the Mediterranean countries to be modulated by meteorology along rather regular seasonal patterns (Mona et al., 2012). For instance, in the Western Mediterranean region the African dust occurrence is higher in summer (Salvador et al., 2014), while in the central Mediterranean region, spring and summer are, usually, associated with dust aerosol loads extending up to altitudes of 3–4 km (Barnaba and Gobbi, 2004). In the Eastern Mediterranean, the main dust transport occurs from spring to autumn (Papayannis et al., 2009; Nisantzi et al., 2015; Soupiona et al., 2018) as a result of the high cyclonic activity over the northern Africa during these periods (Flaounas et al., 2015). Considering also that the Mediterranean basin is a region of high evaporation, low precipitation and remarkable solar activity, the transportation of aerosols accompanied with aging and mixing processes make this area a study of interest for present and future climate change effects (Michaelides et al., 2018).

It is well documented that mineral dust highly influences the atmospheric radiative balance through scattering and absorption processes (direct effect) as well as cloud nucleation, formation and lifetime (indirect effects) as shown in IPCC (2014). Considerable uncertainties in quantifying the global direct radiative effects of aerosols arise from the variability of their spatio-temporal distribution and the aging/mixing processes that can affect their optical, chemical and microphysical properties. Therefore, the magnitude and even the sign of the dust aerosol solar radiative forcing are highly uncertain as they strongly depend on their optical properties, their size distribution and their complex refractive index (CRI) values. Papadimas et al. (2012) reported that the aerosol optical depth seems to be the main parameter for modifying the regional aerosol radiative effects (under cloud-free conditions) and, that on an annual basis, aerosols can induce a significant "planetary" cooling over the broader Mediterranean basin. Other studies (Quijano et al., 2000; Tegen et al., 2010) have shown that the presence of clouds and the surface albedo are also unquestionable parameters affecting the net solar radiative transfer at the top of the atmosphere. However, a comprehensive analysis from ground-based aerosol optical properties to vertical profiles of short- and long-wave radiation estimations in the Mediterranean region has been reported so far only in a few papers (Sicard et al., 2014; Meloni et al., 2003; 2015; Gkikas et al. 2018).

Although there have been a lot of studies about Saharan dust optical properties based on the lidar technique (Papayannis et al., 2009; Mona et al., 2012; Navas-Guzmán et al., 2013; Soupiona et al., 2018), systematic long-term statistical studies are quite scarce since few aerosol depolarization data are available covering long periods. In Pérez et al. (2006) it is proposed that a regional atmospheric dust model, with integrated dust and atmospheric radiation modules, represents a promising approach for further improvements in numerical weather prediction practice and radiative impact assessment over dust-affected areas, especially in the Mediterranean. Hence, an in-depth study of the role of aerosols on the radiative forcing into different regions in the Mediterranean basin is still needed. While a synergy of ground-based lidar measurements and modelling seems very promising for obtaining radiative forcing estimations of dust aerosols, the use of inputs from regional models could also contribute for such estimations in areas where measurements are unavailable.

This paper aims to fill some of the aforementioned gaps by combining statistical lidar data of aerosol optical and microphysical properties with radiative transfer estimations and is organized as follows. A brief summary of the four selected EARLINET Mediterranean stations is given in Sect. 2 along with the data selection of the dust cases. Section 3 includes the description of the methodologies applied and the tools and models used for retrieving the aerosol optical and microphysical properties and their radiative forcing. The evaluation of the retrieved aerosol mass concentration profiles and of the ground level radiation are also presented. The results of the aerosol optical, geometrical and microphysical properties of the individual dust layers and the clusters, as well as the relevant radiative forcing calculations over the studied areas are discussed in Sect.4. Finally, concluding remarks are given in Sect. 5.

2. Instrumentation and data

The European Aerosol Research Lidar Network (EARLINET, https://www.earlinet.org/) established in 2000, provides an excellent opportunity to offer a large collection of quality assured ground-based data of the vertical distribution of the aerosol optical properties over Europe. These measurements meet absolute accuracy standards to achieve the desired confidence in aerosol radiative forcing calculations. Currently, the network includes 31 active lidar stations distributed over Europe, providing information of aerosol vertical distributions on a continental scale. In this paper, level 2 data of four stations from the EARLINET database including aerosol backscatter (β_{aer}) extinction (α_{aer}) coefficient and depolarization ratio (δ_{aer}) profiles as a function of height above mean sea level (a.s.l.) were collected and further analyzed as described below to finally estimate their role in radiative transfer calculations in the Mediterranean region.

2.1. EARLINET stations

Four EARLINET stations affected by typical Saharan dust intrusions in the Mediterranean were selected (listed from West to East): Granada (Spain), Potenza (Italy), Athens (Greece) and Limassol (Cyprus) during a four year (2014–2017) common period of aerosol depolarization Raman lidar data obtained at 532 nm. Table 1 summarizes the basic information about these lidar systems for each location. Except the Limassol station that provides data only at 532 nm, the other three stations are equipped with a depolarization Raman-lidar system able to provide extensive aerosol properties, namely three β_{aer} (355, 532, 1064 nm) and two α_{aer} (355, 532 nm) as well as aerosol intensive properties namely the backscatter and extinction related Ångström exponents ($AE_{\alpha355/532}$, $AE_{\beta355/532}$, $AE_{\beta532/1064}$ nm), the lidar ratio (LR), and additionally the linear volume (δ_{v532}) and particle depolarization ratio (δ_{p532}) at 532 nm. By using the Raman technique, as proposed by Ansmann et al., (1992), we can retrieve the α_{aer} and β_{aer} vertical profiles, with systematic uncertainties of ~5–15% and ~10–25%, respectively (Ansmann et al., 1992; Mattis et al., 2002). Therefore, the corresponding systematic uncertainty of the retrieved lidar ratio values is of the order of 11–30%, while the mean uncertainty for AE_α and AE_β is of order 7–21% and 14–35% respectively, estimated by propagation error calculations.

Table 1: Station name, location, lidar setup and relevant references of the four selected EARLINET stations.

Station	Abbreviation	Location	Lidar setup	References
Andalusian Institute for Earth System Research, University of Granada, Spain	IISTA-CEAMA, **Gr**	37.16º N, -3.61º E, elev. 680 m	MULHACEN $3\beta + 2\alpha + \delta_{p532}$ Overlap: 500 a.g.l.	Guerrero-Rascado et al., 2008
Consiglio Nazionale delleRicerche – Istituto di Metodologie per l'AnalisiAmbientale, Potenza, Italy	CNR-IMAA, **Po**	40.60º N, 15.72º E, elev. 760 m	MUSA $3\beta + 2\alpha + \delta_{p532}$ Overlap: 405 a.g.l.	Madonna et al., 2011
Laser remote Sensing Unit, National Technical University of Athens, Athens, Greece	LRSU-NTUA, **At**	37.96º N, 23.78º E, elev. 212 m	EOLE/AIAS $3\beta + 2\alpha + \delta_{p532}$ Overlap: 800 a.g.l.	Kokkalis, et al., 2012; Soupiona et al., 2019
Cyprus University of Technology, Limassol, Cyprus	CUT, **Lm**	34.67º N, 33.04º E, elev. 10 m	Polarisation Raman lidar, $1\beta + 1\alpha + \delta_p$ (532 nm) Overlap: 250 a.g.l.	Nisantzi et al., 2015

2.2. Selection of dust events

The selection of the lidar dust cases was based on the values of the aerosol optical properties δ_{p532} and LR_{532} (Groß et al., 2013). Since pure dust layers are rare over the Mediterranean cities due to continental contamination by urban, polluted or even biomass burning (BB) aerosols, a sufficiently lower δ_{p532} value with respect to the pure dust values (e.g. Freudenthaler et al., 2009) should be considered to characterize an aerosol layer as a dusty one. Based on previous studies, the respective LR_{532} values for long-range transported mixtures over the Mediterranean area are expected to range between 35-75 sr (Mona et al., 2006; Papayannis et al., 2008; Tesche et al., 2009; Groß et al., 2011; Ansmann et al., 2012; Nisantzi et al., 2015; Soupiona et al., 2018). Consequently, from the total set of

Saharan dust events per station listed in the EARLINET database for the period 2014–2017, we considered for
125   further analysis only the data meeting three basic criteria: a) $\delta_{p532} \geq 0.16$ in the free troposphere, b) 35 sr $\leq$
LR $_{532} \leq$ 75 sr in the free troposphere and c) the thickness of the detected layer to be 500 m, at least. The critical
height (in meters a.s.l.) in which the first criterion was met, was considered to be the base of the dust layer. This
assumption was deemed necessary to be made since usually, the lofted dust layers cannot be distinguished from the
top of the Planetary Boundary layer (PBL), while the presence of urban haze and pollution decreases drastically the
130   δ_p values down to 0.03–0.10 (Gobbi et al., 2000; Groß et al., 2013). The top of the dust layer was estimated as the
height where the signals were similar to the molecular scattering in the free troposphere. For some cases of the
Athens station, where depolarization measurements were unavailable, the values of the base and top were calculated
from the Raman lidar signals, following the procedure proposed by Mona et al. (2006).

Moreover, we performed a careful investigation of the air mass origin and dust transport path by means of
135   backward trajectory analysis. This analysis was carried out using the HYbrid Single-Particle Lagrangian Integrated
Trajectory (HYSPLIT) model (https://ready.arl.noaa.gov/HYSPLIT_traj.php, (Stein et al., 2015) together with the
GDAS (Global Data Analysis System) meteorological files (spatial resolution of 1° × 1°, every 3 hours) as data
input. The kinematic back-trajectories were calculated using the vertical velocity component given by the
meteorological model with a 96–120 hours pathway (4–5 days back). Modis/Terra information
140   (https://firms.modaps.eosdis.nasa.gov/map) was also taken into account for the corresponding hot spots of possible
fires and thermal anomalies along the trajectories (https://firms.modaps.eosdis.nasa.gov/map, not shown here).

Thus, we ended up with 51 individual cases in total (15 for Granada, 18 for Potenza, 12 for Athens and 6 for
Limassol). For the region of Cyprus, the situation is more complex since Middle East dust outbreaks occur also
frequently in addition to the Saharan dust events (Nisantzi et al., 2015; Kokkalis et al., 2018; Solomos et al., 2019).
145   On top of that, dust particles originating from Middle East proved to have different lidar ratio values than the
corresponding observations over Saharan desert (Mamouri et al., 2013; Kim et al., 2020). Taking this into account,
dust cases over the Limassol station originating from Middle East regions were excluded from our study.

The air mass trajectory analysis based on HYSPLIT for each station reveals the origin of each observed layer
(Fig.1). In the majority of cases, air masses originate from the west and northwest Africa (Morocco, Mauritania,
150   Algeria and Tunisia). At a first glance two occurrences seem to dominate: i) trajectories that travel directly from
the source to the observation stations and ii) trajectories that circulate over the Mediterranean or the Atlantic Ocean
(for the Granada cases), Europe and Balkans or even Turkey (for the Limassol cases) before reaching the
observation stations.
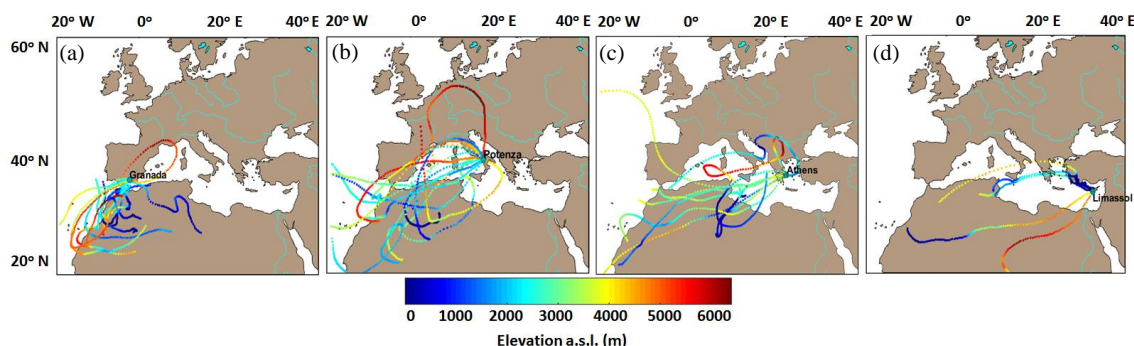
155

Figure 1: 96–120-hour backward trajectories for air masses arriving over a) Granada, b) Potenza, c) Athens and d) Limassol,
for arrival heights of approximately the center of each observed dust layer (51 cases in the period 2014–2017).

3. Methodologies, tools and data evaluation

In order to perform simulations for further investigating the behavior of the transported dust aerosols and their impacts we used different methods with a variety of tools and models. In this section we present our efforts for retrieving vertical dust mass concentration profiles, aerosol microphysical properties and radiative forcing results. Evaluation of the models used was also implemented.

3.1. Dust mass concentration lidar retrievals

To retrieve the aerosol dust mass concentration profiles, we used the β_{532} and the δ_{p532} coefficients. Furthermore, by assuming that we have two aerosol types (dust and non-dust) inside the calculated β_{532} values, we separated the backscatter profiles in two components: the first arising from the contribution of the weakly depolarizing particles ($\delta_{nd} = 0.05$ for non-dust particles) and the second from the contribution of strongly depolarizing particles ($\delta_d = 0.31$ for dust particles). Then, the dust-related backscatter coefficient β_d at 532 nm was obtained, following the procedure described by Tesche et al. (2009). The estimation of the height-resolved mass concentration (in kg m^{-3}) of dust particles was based on the procedure described by Ansmann et al. (2012), using the following equation,

$$mass_d = \rho_d (v_d/\tau_d)\beta_d \, LR_d \qquad (1)$$

where in our study the coarse-particle mass density (ρ_d) was assumed equal to 2.6 gm^{-3} and a mean volume-to-AOT ratio for coarse mode particles, v_d/τ_d was calculated from AERONET measurements (https://aeronet.gsfc.nasa.gov/) for each station during the period 2014–2017. We report these values as follows: 0.71 ± 0.37 μm for Potenza, 0.80 ± 0.29 μm for Granada, 0.94 ± 0.50 μm for Athens, and 0.87 ± 0.27 μm for Limassol. The mean values of the whole studied period were calculated, since only few of the studied cases were common in EARLINET and AERONET database. For LR$_d$ the mean values of 52 ± 8 sr, 51 ± 9, 52 ± 9 sr and 49 ± 6 sr were used per site, respectively as calculated from our findings.

3.2. The Spheroidal Inversion eXperiments (SphInX) software tool

The SphInX software provides an automated process to carry out microphysical retrievals from synthetic and real lidar data inputs and further to evaluate statistically the inversion outcomes. It has been developed at the University of Potsdam (Samaras, 2016) within the Initial Training for atmospheric Remote Sensing (ITaRS) project (2012–2016). The methodology applied here for spheroid-particle approximation is the same as presented in Soupiona et al. (2019). Raman lidar observations were used as inputs for specific heights within the layers and averaged to produce the 6-point dataset of the so-called $3\beta_{par} + 2\alpha_{par} + 1\delta$ setup. All cases fulfilling this setup were treated in parallel for retrieving their microphysical properties. The CRI grid was narrowed down to [1.4, 1.5] for the Real part (RRI), and [0, 0.001, 0.005, 0.01] for the Imaginary part (IRI), while radius R$_{eff}$ ∈ [0.01, 2.2] in μm. The outputs presented here are the RRI and IRI, the Single Scattering Albedo (SSA) and the effective radius (R$_{eff}$).

3.3. Atmospheric dust cycle model (BCS-DREAM8b)

The BSC-DREAM8b model (Basart et al., 2012), operated by the Barcelona Supercomputer Center (BSC-CNS: www.bsc.es) provides operational forecasts since May 2009, is also participating in the northern Africa-Middle East-Europe (NA-ME-E) node of the SDS-WAS program. The BSC-DREAM8b is a regional model designed to simulate and predict the atmospheric cycle of mineral dust aerosols. It is one of the most widely used and evaluated models for dust studies over northern Africa and Europe (cf. Jiménez-Guerrero et al., 2008; Papayannis et al., 2009; Basart et al., 2012; Amiridis et al., 2013; Tsekeri et al., 2017). The present analysis includes vertical profiles of dust mass concentration simulations (0.3º x 0.3º horizontal resolution, 24 vertical levels, corresponding to the studied cases and for time periods close to the measurement times, usually at 18:00 and 00:00

200 UTC, since the meteorological fields are initialized every 24h (at 12:00 UTC) with the NCEP global analysis (0.5°x0.5°) and the boundary conditions are updated every 6h with the NCEP GFS forecasts (0.5°x0.5°).

3.4. Radiative forcing simulations

The aerosol effects on solar and terrestrial radiation are usually quantified through the so-called aerosol radiative forcing (ARF). The dust radiative forcing (DRF) defined here as the perturbation in flux in the atmosphere
205 caused by the presence of the dust aerosols in relation to that calculated under clear sky conditions, can be expressed as (Quijano et al., 2000; Sicard et al., 2014; Mishra et al., 2014):

$$DRF(z) = \Delta F^{dust}(z) - \Delta F^{clear}(z) \quad (2)$$

where, the net flux, ΔF at a level z, is the difference between the downwelling, and upwelling flux, $F\downarrow$ and $F\uparrow$, respectively:

210
$$\Delta F(z) = F\downarrow(z) - F\uparrow(z) \quad (3)$$

These fluxes (in W m⁻²) are calculated separately for SW and LW radiation sources and assuming that the amount of the incoming solar radiation at the TOA is equal for both cases with and without the presence of dust aerosols. Therefore, the net DRF, $DRF_{NET}(z)$, is expressed as:

$$DRF_{NET}(z) = DRF_{SW}(z) + DRF_{LW}(z) \quad (4)$$

215 Based on this definition, the DRF at a given altitude will be positive when the aerosols cause a heating effect and negative when they cause a cooling effect. Finally, the DRF within the atmosphere (DRF_{Atm}) can be defined as the net difference between DRF at the top of the atmosphere (TOA) and the bottom of the atmosphere (BOA), denoted here as DRF_{TOA} and DRF_{BOA}, respectively:

$$DRF_{Atm} = DRF_{TOA} - DRF_{BOA} \quad (5)$$

220 Our analysis was based on these equations for estimating the radiative forcing by means of direct and diffuse irradiances of an accurate radiative transfer model combining lidar measurements and dust concentration simulations.

3.4.1. The radiative transfer model (LibRadtran)

In this study, the downwelling and upwelling shortwave (280-2500 nm) and longwave (2.5-40 μm)
225 irradiances at TOA and BOA levels have been simulated with the LibRadtran radiative transfer model version 2.0.2. (Emde et al., 2016). This software package contains numerous tools to perform various aspects of atmospheric radiative transfer calculations. In our study, the *uvspec* program that calculates the radiation field in the Earth's atmosphere was implemented for the *disort* radiative transfer equation (1-D geometry). Mid-latitude conditions (AFGL Atmospheric Constituent Profiles, 0–120 km) and a typical surface albedo value (0.16) for urban areas
230 (Dhakal, 2002) in the SW range were taken into account based also on visual observations. The OPAC library 4.0 (Koepke et al., 2015) was used for desert spheroids (T-matrix calculations) to determine aerosols' radiative properties in the aforementioned wavelength ranges. The non-spherical approximation is given by typical particle size dependent aspect ratio distributions of spheroids, derived from measurements at observation campaigns. In our study, the mineral particles of each case are given to the model as spheroids for the mineral accumulation mode
235 (MIAM) with $R_{MIAM} \in [0.005, 20]$ in μm.

A set of four simulations was carried out per case of the studied dust events. The first two simulations refer to clear-sky atmospheres with background/baseline aerosol conditions (default properties: rural type aerosol in the boundary layer, background aerosol above 2 km, spring-summer conditions and a visibility of 50 km), for SW and for LW range, treated separately. The other two simulations correspond to dust loaded atmosphere, also in SW and
240 LW ranges, respectively, for which vertical profiles of different components of dust layers were used as additional

inputs. These inputs have been obtained with three different Schemes: A) vertical mass concentration profiles simulated by the BCS-DREAM8b model, B) vertical dust mass concentration profiles retrieved based on the β_{532} and δ_{p532} profiles, and, C) vertical profiles of α_{532} along with the respective mean AOT_{532} value. The flow chart in Fig. 2 depicts these three Schemes applied to create the input files for the dust-loaded atmospheric conditions used in LibRadtran software package (Emde et al., 2016). For Scheme C conversion factors from OPAC were used in order to convert the α_{par} and the corresponding AOT from 532 nm to 10 μm (peak, within the atmospheric window). The conversion was based on an adaptive inversion algorithm of Shang et al. (2018) who presented a way to convert extinction coefficients at different wavelengths by using Angstrom exponent values derived from AOTs.

For all these Schemes in this study, 30 vertical levels have been used between ground and 120 km height with a spatial vertical resolution of 0.5 km starting from ground level (BOA) to 2 km and from 5 to 10 km, a resolution of 0.2 km from 2 to 5 km, due to the presence of the dust layers within this height range and additionally at the heights of 20 and 120 km (TOA). All simulations were performed for three different Solar Zenith Angles (SZA), 25° 45° and 65° covering a typical diurnal cycle for radiative forcing estimates at mid-latitudes. All cases were treated for cloud-free conditions. Except the altitude in km (z_{out}), the additional outputs that have been implemented in our Schemes are: the direct horizontal irradiance (e_{dir}), the global irradiance (e_{glo}) the diffuse downward irradiance (e_{dn}), the diffuse upward irradiance (e_{up}), and the heating rates (heat) in K day^{-1}, as described by Mayer et al. (2017).
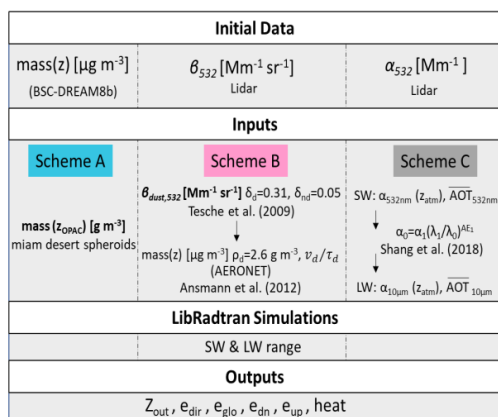
Figure 2: Flowchart of the three Schemes used to retrieve simulations of irradiances using the LibRadtran software package.

3.4.2. Radiation data set

LibRadtran irradiance outputs have been validated against reference solar irradiance pyranometer measurements at the Earth's surface (Kosmopoulos et al., 2018). For this study, solar radiation data measured by pyranometers were available only for the Granada and Athens stations. The reference solar radiation data set consists of one-minute simultaneous measurements of horizontal global and diffuse irradiance measured with two CMP11 pyranometers, at Granada, and two CMP21, at Athens (NOA's actinometric station in Penteli area). These pyranometer models, both manufactured by Kipp & Zonen, have a black-coated thermopile acting as a sensor which is protected against the meteorological conditions by two concentric hemi-spherical domes. They both comply with the International Organization for Standardization (ISO) 9060 (1990) criteria for an ISO secondary standard pyranometer, being classified as "high quality" according to the World Meteorological Organization (WMO) nomenclature (WMO, 2018). Additionally, the corresponding pyranometer measuring the diffuse component was mounted on a shading device to block the direct irradiance and prevent it from reaching the sensor. In this study, the shading devices employed were a Solys2 sun tracker and a CM121 shadow ring, at Granada and Athens

respectively, both manufactured by Kipp & Zonen. For those diffuse irradiance measurements taken using a shadow ring, the model proposed by Drummond (1956) has been apply in order to correct for the diffuse radiation intercepted by the ring, as suggested the manufacturer (Kipp & Zonen, 2004).

3.5. Evaluation of aerosol mass concentration vertical profiles

Before using the aerosol mass concentrations vertical profiles from i) BSC-DREAM8b model simulations (Scheme A) and ii) hourly averaged lidar measurements (Scheme B) as inputs to the LibRadtran model, we performed a day-by-day comparison between them. Due to the different spatial vertical resolution between the modeled and the lidar profiles, both profiles were degraded to the fixed height levels of the OPAC dataset (0, 1, 2, 3, 4, 5, 6, 7, 8, 9, 10, 11, 12, 35 km).

Figure 3 shows the Taylor's diagram of the mass concentration simulated by the BSC-DREAM8b model against the lidar-retrieved ones. The azimuthal angle presents the correlation coefficient; the radial distance presents the normalized SD of the simulated patterns, the distance from the point on the x-axis presents the root mean square error (RMSE), while the black point at the (1,1) cross section, indicates the lidar retrieved aerosol mass values representing the reference point. The normalization of the SD is performed with respect to the calculated values. It is evident that the shape of the vertical distribution was better reproduced than the intensity of each event. Specifically, in the 66 % of the cases there is a good correlation ($r > 0.6$), in the shape of the vertical distribution, while in 96 % of the cases the model gives lower concentration values (*normalized SD* < 1). Therefore, we report a mean underestimation of the mean mass concentration values of the BSC-DREAM8b of the order of 31%. Also, the mean center of mass (in km) estimated from BSC-DREAM8b profiles is 0.6 km lower than the one calculated from the lidar measurements (2.6 ± 1.0 km and 3.2 ± 1.1 km respectively). However, we should take into consideration: i) the spatial resolution, where the lidar observations are considered as point measurements while the simulations represent uniform pixels of 0.3º resolution and ii) the temporal resolution, where the lidar retrieved profiles are hourly averaged, while the model derived profiles are instantaneous results, saved every 6 hours. Therefore, our observations are in line with previous studies of Mona et al. (2014) and Binietoglou et al. (2015) where have reported discrepancies concerning the base, the top layer height and extinction profiles and good agreement in terms of profile shape, between the BSC-DREAM8b and observations.
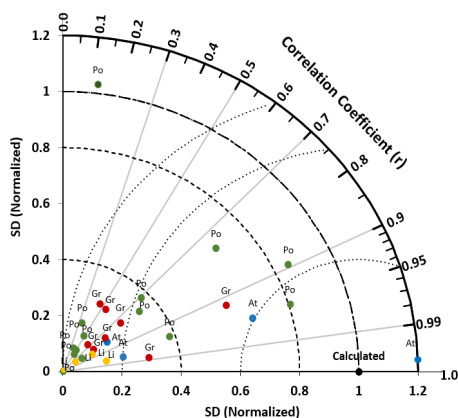
Figure 3: Taylor's diagram of the case-by-case vertical mass concentration simulated by BSC-DREAM8b model against the lidar retrieved ones.

3.6. Evaluation of ground level LibRadtran outputs

The evaluation of the performance of the model was undertaken by statistical means. The relative root mean square error (rRMSE), the relative mean bias error (rMBE) the correlation coefficient (r) and the normalized SD

were calculated in order to numerically quantify the performance of the global irradiance calculated from pyranometers and simulated from the three Schemes. Table 2 shows the statistical results for the modeled global irradiance values versus the reference pyranometer measurements for both locations and the threes schemes. All scheme simulations perform remarkably well, with rRMSE values ranging from 8.3 to 16.2% and rMBE values between 0 and 15.2%. In general, the rRMSE is slightly higher at Granada, mainly for the Scheme A. According to this statistic, the LibRadtran output with the best performance are those obtained with the Scheme C as input followed by Scheme B and A, respectively. This order is the same attending to the rMBE values with the exception of the Scheme A at Athens. The correlation coefficient r depicts the good performance of the radiative transfer model for the three schemes and the two locations models. All simulations present a $r > 0.95$ with minor differences (below a 10%) in the normalized SD values respect to the pyranometer global irradiance values. A slight overestimation is observed for all scheme outputs at Granada (norm SD > 1). Conversely, this overestimation is no longer evident in the modeled global irradiance for Athens. It is important to notice the good performance of the Scheme B despite the important calculus involved in it.

Table 2: Statistical metrics for the modeled global irradiance values versus the reference pyranometer measurements for Granada and Athens and the threes schemes applied.

	Granada				Athens			
	rRMSE (%)	rMBE (%)	r	SD (norm)	rRMSE (%)	rMBE (%)	r	SD (norm)
Scheme A	16.2	15.2	0.99	1.09	10.8	- 0.2	0.97	0.89
Scheme B	11.9	5.7	0.97	1.10	10.2	8.3	0.99	0.92
Scheme C	8.8	5.9	0.99	1.09	8.3	6.3	0.99	0.96

4. Results

4.1. Aerosol geometrical and optical properties per site

For each case studied, the mean δ_{p532}, mean LR_{532} and mean AOT_{532} values were calculated inside the dust layers as shown in Fig.4 (a-d). The corresponding standard deviation (SD) values give an indication of the variability of these parameters from base to the top of the dust layer. Figure 4a shows the aerosol geometrical properties for the detected layers one by one, per station and per year. The mean values of the base and top height of the dust layers per station, along with their SD are marked with horizontal bounded lines. At the four sites (Granada, Potenza, Athens and Limassol) mean layer thicknesses of 3392 ± 1458 m, 2150 ± 1082 m, 1872 ± 816 m and 1716 ± 567 m were calculated respectively. We also found mean δ_{p532} values of 0.24 ± 0.05, 0.26 ± 0.06, 0.28 ± 0.05 and 0.28 ± 0.04 (Fig. 4b), and mean AOT_{532} values of 0.40 ± 0.31, 0.11 ± 0.07, 0.12 ± 0.10 and 0.32 ± 0.17 (Fig. 4d), respectively. Similar mean LR_{532} values of around 51 sr (Fig. 4c) were found for all stations. The Granada station holds the minimum mean value for layers' base height (1567 ± 788 m) and the maximum for top height (4960 ± 975 m) and layer's thickness. Concerning the LR values no remarkable deviations were observed among the four stations having mean values around 50 sr, which are in very good agreement with literature findings (Tesche et al., 2009; Ansmann et al., 2012; Groß et al., 2011; 2013). The largest mean AOT value, equal to 0.40 ± 0.31, observed over Granada station is in accordance to the geometrical properties of Fig.4Figure a that depicts thick dust layers in the majority of the cases.
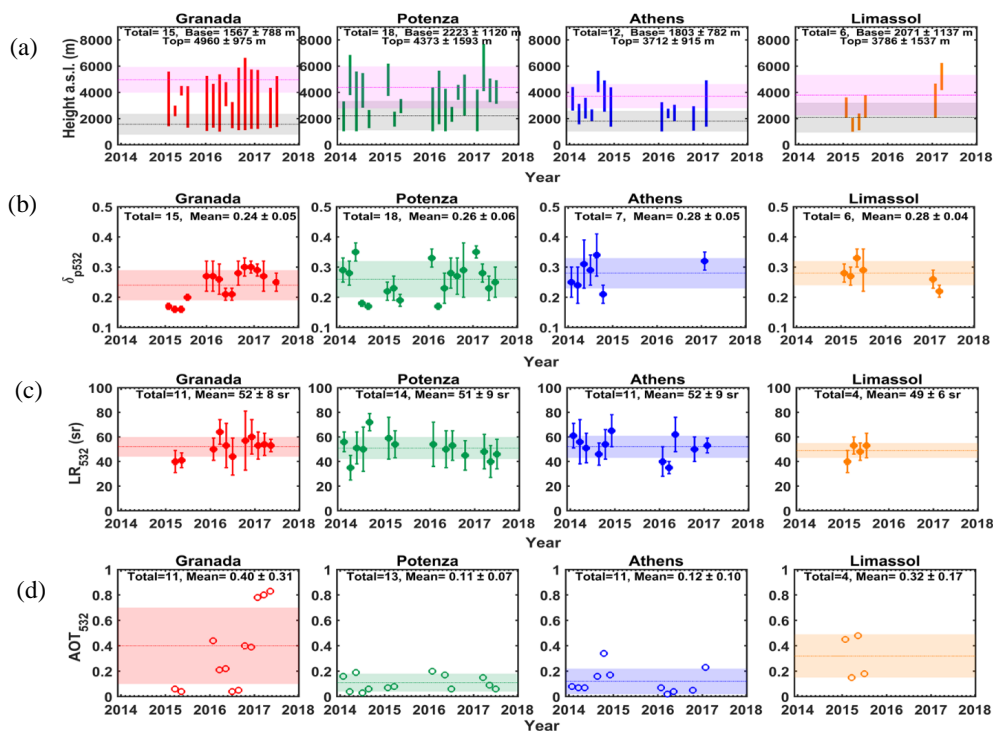
Figure 4: Mean values along with standard deviation of a) base and top, b) δ_{p532}, c) LR_{532} and d) AOT_{532}, per station (text and banded lines) and per case (symbols and error bars) inside the observed dust layers.

Considering Granada's station as representative of the west Mediterranean region, Potenza of the central Mediterranean region, Athens and Limassol stations of the eastern Mediterranean region, a dust aerosol mode classification per region can be made. For this purpose, the mean AOT_{532} versus the $AE_{\beta532/1064}$ giving an indication of the aerosol particle size in the atmospheric column relevant to the aerosol load for each region are shown in Fig. 5. A wide spread of the AOT values at moderate to low $AE_{\beta532/1064}$ values (between 0 and 0.6) observed in the Western Mediterranean region, demonstrates that the dust size distribution in this area is dominated by coarse mode particles during events of different intensities. On the other hand, the presence of dust layers, in the central and eastern Mediterranean regions can be associated with higher $AE_{\beta532/1064}$ values (even up to 1.5) and consequently, with the presence of fine mode particles and lower dust loads. Our findings verify that the longer the dust transport is, more likely it is for the dust aerosol properties to be modified, since dust can frequently be mixed with background aerosols in the eastern Mediterranean (Groß et al., 2019).

In terms of the aerosol size distribution, the scatter plot of Fig. 5 allowed us to perform a k-means clustering (Arthur and Vassilvitskii, 2007) in order to define three physically interpretable aerosol size distributions: a) fine mode, with $AE_{\beta532/1064} > 0.6$, b) coarse mode, with $AE_{\beta532/1064} \leq 0.6$ and AOT_{532} between 0 and 0.2, c) whilst $AE_{\beta532/1064}$ values smaller than 0.6 attributed to large AOTs (between 0.2 and 0.8) are representative of extreme dust events. It seems that the majority of these extreme dust outbreaks occur over the Western Mediterranean region, more likely due to its location close to the African continent. For example, Fernández et al. (2019) recently reported an unprecedented extreme winter time Saharan dust event, during February 2017, over the whole Iberian Peninsula

360   with AOTs > 0.2 (675 nm) and *AE* values around zero. More studies referring to the occurrence of extreme dust events over the aforementioned area can be found in literature (Cachorro et al., 2008; Guerrero-Rascado et al., 2009).
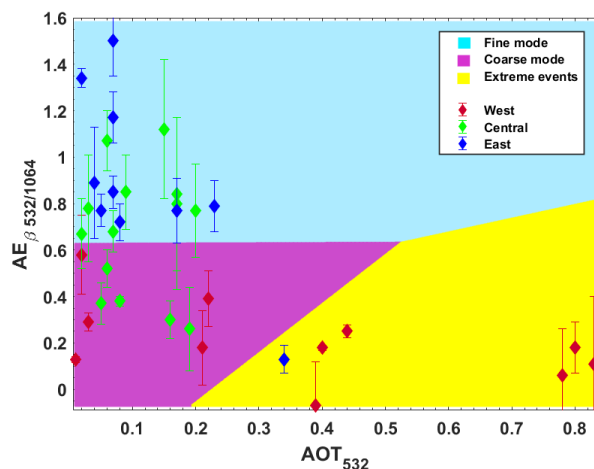
Figure 5: $AE_{\beta532/1064}$ versus AOT_{532} per region: west (red marks and error bars), central (green marks and error bars) and east (blue marks and error bars) Mediterranean region. K-means clustering revealed three clusters: fine mode (ciel background), 365   coarse mode (magenda background) and extreme dust events (yellow background).

4.2. Clustering per mixing state

Based on the High Spectral Resolution Lidar (HSRL) classification presented by Groß et al. (2013), we plotted the intensive aerosol quantities LR_{532} versus δ_{p532} and we identified three of the six existing clusters in our data (Fig 6). The first cluster (green marks and error bars) represents a mixing state of Saharan dust and BB aerosols 370   having a large spreading in mean LR values and low mean δ_{p532} values (40 sr ≤ LR_{532} ≤ 75 sr, 0.15 ≤ δ_{p532} ≤ 0.19). The second one, (red marks and error bars) is attributed to mixed Saharan dust, where dust aerosols are dominant, but urban/continental, marine or even pollen aerosols are also possibly present (40 sr ≤ LR_{532} ≤65 sr, 0.20 ≤ δ_{p532} ≤ 0.29). The third cluster (orange marks and error bars) is attributed to pure Saharan dust aerosols (45 sr ≤ LR_{532} ≤ 60 sr, 0.30 ≤ δ_{p532} ≤ 0.36). The most populated and consequently, the most common, among 375   those three clusters is the red one, as expected, due to the frequent mixing of dust aerosols with continental ones (Papayannis et al, 2008). The range of our measured δ_{p532} values as indicated with the horizontal error bars in Fig. 6, overlap between the three identified aerosol clusters, showing a more realistic transition from one cluster to the other, bridging the gap specifically between green and red clusters from the HSRL classification.
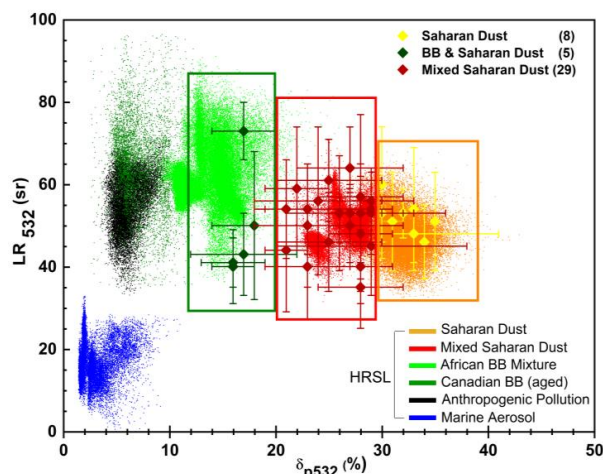
Figure 6: LR_{532} versus δ_{p532} values from HSRL observations presented by Groß et al. (2013), (colored dots) along with the selected datasets from the four EARLINET stations (symbols and error bars).

Table 3 summarizes the mean values of the aerosol geometrical, optical, and microphysical properties of the three identified clusters. A synergistic approach of HYSPLIT (trajectories of 120 hours backward for each case) and Google Earth (distance calculator) allowed us to estimate the distance travelled (in km) to the respective sites and the mixing hours per cluster. Specifically, the term of mixing refers to the hours the air masses travelled after leaving the African continent. We can see that the Saharan dust cluster of the air masses that present the lowest mixing with other air masses (26 ± 13 hours), compared to the other clusters (41 ± 26 hours for the BB & mixtures and 31 ± 13 hours for the mixed Saharan dust cluster). Moreover, the air masses of the Saharan dust cluster seem to travel faster than those of the other clusters, although covering a greater distance (4845 ± 2825 km) at the same time (within 120 hours). Now, the main difference between the two remaining clusters (BB & mixtures/Mixed Saharan Dust) is attributed to the mixing hours. The air masses of the latter cluster remain 15 hours longer and circulate over the Mediterranean and Europe, so they are probably enriched with other types of aerosols.

Concerning the aerosol optical properties, the β_{532} and α_{532} show lower values for BB & dust and for mixed Saharan dust cases ($1.10 \pm 0.15 \ x10^{-3} km^{-1}sr^{-1}$, $0.47 \pm 0.28 \ km^{-1}$ and $1.24 \pm 0.80 \ x10^{-3} km^{-1}sr^{-1}$, $0.74 \pm 0.48 \ km^{-1}$ respectively) and higher values ($1.54 \pm 1.05 \ x10^{-3} \ km^{-1}sr^{-1}$, $0.80 \pm 0.27 \ km^{-1}$) for the Saharan dust cluster. Therefore, higher AOT values (0.32 ± 0.25) were found for the latter cluster compared to the others, due to the higher dust burden of these events over the affected sites. The highest δ_{p532} values (0.32 ± 0.02), indicate the arid origin and the coarse mode of pure Saharan dust layers (Freudenthaler et al., 2009) of the corresponding cluster. No direct information can be extracted from the similar LR_{532} values about the mixing state of the aerosol layer, except that the range of the SD narrows as the mixing decreases. However, for the cases that observations at 355 nm were available, it seems that the lidar ratio color ratio (namely the LR_{355}/LR_{532}) converges to unit for the Saharan Dust cluster, indicating the absence of spectral dependence for the case of pure dust (Müller et al., 2007; Veselovskii et al., 2020). For these cases also, the $AE_{\beta 355/532}$ becomes closer to zero taking mean value of 0.35 ± 0.45.

We also summarise the changes in mean microphysical properties estimated with SphInX for the three identified clusters. The BB & Saharan dust cluster takes the lower mean R_{eff} value (0.293 ± 0.074 μm) due to the fine structure of BB aerosols included in the layer, while a mean R_{eff} of 0.360 ± 0.081 μm corresponds to the cluster of mixed Saharan dust and a slightly larger value (0.387 ± 0.070 μm) corresponds to the Saharan dust cluster. The values for RRI, IRI and SSA at 532 nm were similar for the two clusters that not include BB aerosols, whilst the presence of BB aerosols of the first cluster leads to higher RRI and IRI values and lower SSA, results

410   that are in good agreement with the ones reported in Petzold et al. (2011) over Dakar, for mineral dust and dust mixed with anthropogenic pollution.

Table 3: Mean values of optical, geometrical and microphysical properties of the three identified clusters. The term of mixing refers to the hours the air masses travelled after leaving the African continent.

Parameters		Clusters		
		BB & Saharan Dust	Mixed Saharan Dust	Saharan Dust
Optical Properties	β_{532} (km^{-1}sr^{-1})	1.10±0.15 [x10^{-3}]	1.24±0.80 [x10^{-3}]	1.54±1.05 [x10^{-3}]
	α_{532} (km^{-1})	0.47±0.28	0.74±0.48	0.80±0.27
	LR$_{532}$ (sr)	51 ± 15	50 ± 7	52 ± 5
	δ_{p532}	0.17 ± 0.01	0.26 ± 0.03	0.32 ± 0.02
	LR$_{355}$/LR$_{532}$	0.69 ± 0.24	0.84 ± 0.16	0.98 ± 0.16
	AE$_{\beta355/532}$	0.44 ± 0.59	0.52 ± 0.61	0.35 ± 0.45
	AOT$_{532}$	0.03 ± 0.02	0.15 ± 0.10	0.32 ± 0.25
Geometry & Mixing	Thickness (km)	0.79 ± 0.21	2.08 ± 0.76	3.10 ± 1.72
	Distance (km)	3496 ± 1185	3662 ± 1617	4845 ± 2825
	Mixing (hours)	41 ± 26	66 ± 41	26 ± 13
Microphysical Properties	R$_{eff}$ (μm)	0.293 ± 0.074	0.360 ± 0.081	0.387 ± 0.070
	RRI	1.50 ± 0.00	1.47 ± 0.05	1.47 ± 0.05
	IRI	0.005 ± 0.000	0.0046 ± 0.0045	0.0041 ± 0.0018
	SSA$_{532}$	0.948 ± 0.002	0.964± 0.018	0.964 ± 0.022
	SSA$_{355}$	0.937 ±0.007	0.958 ± 0.022	0.952 ± 0.026

4.3. Regional dust solar radiative forcing (DRF)

415

        As mentioned previously, there is shortage of papers in the literature about the role of dust on the Earth's radiation budget. Since very few in situ direct measurements of DRF effects and heat fluxes are available especially in the Mediterranean (Bauer et al., 2011; Meloni et al., 2018) we are restricted to perform simulations to quantify the role of dust aerosols on the radiative forcing in the studied regions. The mean DRF is calculated during this
420   simulation, calling twice the LibRadtran radiation code: with and without dust aerosols. For all cases the vertical profile of DRF starting from ground level/bottom of atmosphere (BOA) up to the top of atmosphere (TOA) in the SW and LW ranges were simulated using the three aforementioned Schemes.

        A negative forcing of aerosols both at the BOA and TOA is noted in the SW range, as presented in Fig. 7Figure a, which depicts the mean DRF of all cases per scheme. All results within the SW range represent less
425   absorbing aerosols with a cooling behavior. Depending on the dust optical properties and load intensity, DRF values at the BOA range from -40 to -13 W m^{-2} at SZA 25°, from -43 to -14 W m^{-2} at SZA 45° and from -44 to -15 W m^{-2} at 65°. At the TOA, the corresponding ranges per SZA are -9.5 to -1.4 W m^{-2} (25°), -16 to -3.3 W m^{-2} (45°) and -24.3 to -6.9 W m^{-2} (65°). Similarly, in the SZA independent LW range (thermal spectral range), the DRF values range from +1.6 to +4.6 W m^{-2} for the BOA and from +0.8 to +3.6 W m^{-2} for the TOA. Our estimations are consistent
430   with results obtained by other literature findings for Saharan dust aerosols over the Mediterranean region. Specifically, Sicard et al. (2014) found that the SW RF at the BOA has always a cooling effect varying from -93.1 to -0.5 W m^{-2} while the corresponding LW RF has always a heating effect varying from +2.8 to +10.2 W m^{-2}. They also concluded that dust aerosols at the TOA have a cooling effect in the SW spectral range with a RF ranging from -24.6 to -1.3 W m^{-2} while at the TOA the LW RF varies between +0.6 and +5.8 W m^{-2}. Meloni et al. (2003) found
435   at the island of Lampedusa instantaneous RF of -70.8 W m^{-2} at the BOA and -7.5 W m^{-2} at the TOA within the range 300-800 nm for an event with AOT of 0.51 at 415 nm. For the same location and for another strong Saharan dust outbreak (AOT$_{500}$=0.59), Meloni et al. (2015) reported a total (SW + LW) radiative forcing of -48.9 W m^{-2} at the BOA, -40.5 W m^{-2} at TOA, and +8.4 W m^{-2} in the atmosphere for SZA=55.1°. A negative radiative effect

reaching down to -34.8 W m^{-2} at the surface in the Mediterranean area was also recently reported by Gkikas et al.
440   (2018) during the forecast period March 2000–February 2013.

Variations among these values are expected since they strongly depend on the different aerosol AOTs, mass estimations and extinction values. Estimations retrieved from Scheme B are expected to give higher values compared to those given from Scheme A as revealed also by Fig.3. The DRF at the LW spectral region is opposite in sign and significantly lower in absolute values than in the SW region. The difference between the TOA and BOA
445   DRF, with the former to be only weakly perturbed and the latter to be quite stronger, can be attributed to the heating within the troposphere, since the presence of the dust mainly leads to a displace of surface's radiative heating into the dust layer. Low reflected solar flux is partially offset by the absorption of upwelling LW radiation. Finally, in the LW spectral region, the mean DRF values at the BOA (Scheme A: +1.6±1.6 W m^{-2}, Scheme B: +4.6±4.7 W m^{-2}, and Scheme C: +2.9±9.4 W m^{-2}) are higher than those at the TOA (Scheme A: +0.8±0.9 W m^{-2}, Scheme B:
450   +3.6±4.4 W m^{-2}, and Scheme C: +1.2±6.2 W m^{-2}) due to the fact that the main source of LW radiation (Earth's surface) is close to the aerosol layers, mainly observed between 2 and 4 km a.s.l.. As a result, the DRF$_{Atm}$ is positive during the diurnal circle, yielding net radiative heating of the dust layer.

The mean net heating rate within the atmosphere, calculated by adding algebraically both rates in the SW and LW spectral ranges is presented in Fig. 7b. Here, the net heating rate is clearly dependent on the available solar
455   radiation, that increases with SZA due to the low incoming solar radiation reaching the BOA at afternoon hours (SZA 65°). Our estimations are in accordance with the fact that as the SZA increases, the optical path of the SW radiation grows significantly, increasing the attenuation of the direct radiation while generating a higher fraction of the diffuse radiation. This effect is more pronounced at the BOA, in which, the intensity of the heating rate is reduced with increasing SZA, since fewer photons are available to heat the dust layers. The net heating rate values
460   for Scheme A are: -0.05±0.04 K day^{-1} (25°), -0.04±0.03 K day^{-1} (45°) and 0.00±0.02 K day^{-1} (65°). Similar to slightly higher values are observed for Scheme B as follow: -0.07±0.06 K day^{-1} (25°), -0.04±0.03 K day^{-1} (45°), and -0.02±0.02 K day^{-1} (65°). For Scheme C, we report higher values of this parameter during the diurnal circle. More precisely, the net heating rate is almost 1.5 times higher at 25°, 2 times higher at 45° and around 0.8 times higher at 65°, compared to the aforementioned Schemes. Greater sensitivity in the SZA appears in Scheme B as it results
465   from the line slope.
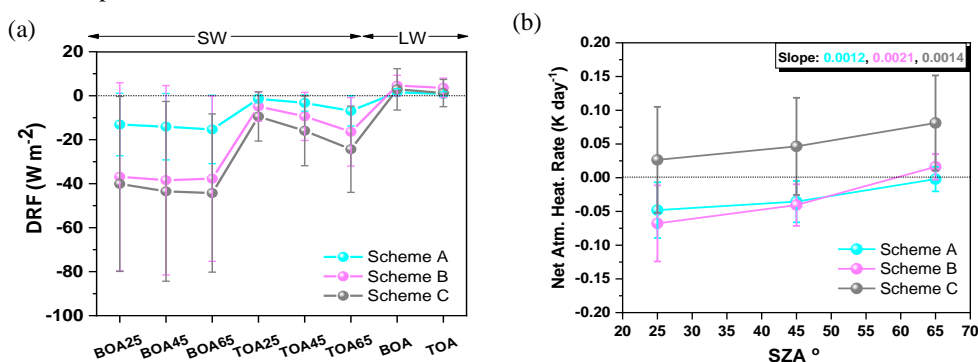
Figure 7: Mean values of a) SW and LW DRF at BOA and TOA and b) the net heating rate within the atmosphere, along with their SD for the three Schemes applied in the total set of the studied cases. The inserted box depicts the line slope.

In order to further explain the difference of sign in the net heating rate of Scheme C, compared to the two
470   others presented in Fig. 7b, we plotted the aforementioned parameter along with the base layer height, the AOT$_{532}$ and the layer thickness of each case as presented in Fig. 8. Taking into account that the effect of net heating rate of the vertical distributions, from negative to positive values, is more pronounced close to surface at small SZA values, the estimations of BOA at 25° SZA were selected to be presented in this graph. It becomes clear that the sign of the

net heating rate at BOA depends on the dust vertical structure and the AOT. More precisely, the majority of the
cases having low AOT_{532} values (≤ 0.2) and low layer thickness (≤ 2 km) give negative net heating rate values.
Additionally, the higher the AOT the higher the absolute value of the net heating rate. Concerning the base layer
height, it plays a key role to the absolute net heating rate of each case, since dust layers close to the ground take
higher absolute net heating rate values. For example, a dust event with base of 2.8 km, 0.73 km thickness and
AOT_{532} equal to 0.01 has a heating rate of -0.17 K day^{-1}, while a layer with base of 3.8 km, 0.66 km thickness and
AOT_{532} equal to 0.02 has a net heating rate of almost zero (-0.03 K day^{-1}). Both the events occurred during the
same month (August). In another comparison, net heating rate values of -0.02 K day^{-1} versus +0.09 K day^{-1} are
reported for two layers, during summer time that have almost the same base (2.6 km and 2.5 km) and thickness (2.3
km and 2.4 km) but different AOT_{532} values (0.08 and 0.34 respectively). Finally, a combination of high AOT_{532}
($0.21 - 0.83$) and high thickness ($2.1 - 5.5$ km), two parameters that are usually directly dependent, along with
low base height ($1.0 - 1.5$ km), give high net heating rate values with positive sign ranging from $+0.06$ to $+0.26$
K day^{-1}.
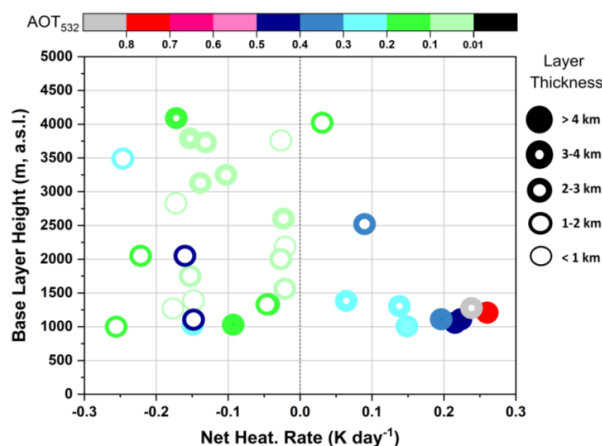
Figure 8: Net heating rate values per case of Scheme C estimated at BOA, 25º SZA versus base layer height. The horizontal
colorbar indicates the AOT_{532} values and the vertical symbol thickness indicates the layer thickness.

Figures 9 (a-c) depicts the same results as in Fig. 7a but for each of the three identified clusters: BB and dust,
mixed Saharan dust Saharan dust. The DRF in the SW range is negative both in the BOA and TOA for all clusters
and is dominated by large dust particles of the Saharan dust episodes (Fig. 9c, Scheme A: -22.5±16.7 W m^{-2}, Scheme
B: -34.0±37.0 W m^{-2}, Scheme C: -49.2±50.9 m^{-2} for BOA, and Scheme A: -2.5±2.1 W m^{-2}, Scheme B: -4.4±5.2 W
m^{-2}, Scheme C: -12.1±14.4 m^{-2} for TOA, SZA 25º), whereas mixed layer with biomass burning aerosols have
significantly lower cooling effect (Fig. 9a, Scheme A: -6.2±4.0 W m^{-2}, Scheme B: -19±9 W m^{-2}, Scheme C: -4.8±3.5
W m^{-2} for BOA, and Scheme A: -0.5±0.4 W m^{-2}, Scheme B: -2.0±1.3 W m^{-2}, Scheme C: -0.7±0.5 m^{-2} for TOA, SZA
25º) for each of the three applied Schemes. DRF seems to be inversely proportional to the mixing ratio, since higher
absolute values are estimated for less mixed dust layers. This can directly be linked to the fact that RF values
strongly depend on α_{par}, β_{par} and AOT that take much higher values for the Saharan dust cluster as already reported
(Table 3). Focusing on the SW range, the cooling effect for Scheme A of the Saharan dust cluster is up to 3 times
higher compared to the BB and Saharan dust one, whilst the cooling effect for Scheme C of the former cluster is up
to 10 times higher compared to the latter. The cooling effect of Scheme B becomes also stronger with the decreasing
mixing state but in a lower magnitude (the former cluster is almost 2 times higher compared to the latter). Hence,
even though the cases included in the Saharan dust cluster usually take higher mass concentration values than the
other cases, as predicted by BSC-DREAM8b (Scheme A), still it seemingly underestimates the intensity of strong

transported dust episodes over the observation stations. On the contrary, Scheme C is the most sensitive to the mixing state. To explain this result one should consider that on the one hand, spheroidal particles such as dust have larger surface area than spherical ones such as BB aerosols leading to larger AOTs (Haapanala et al., 2012) and consequently to increased negative DRF and on the other hand, the Schemes A and B involve greater assumptions concerning dust particles than Scheme C.
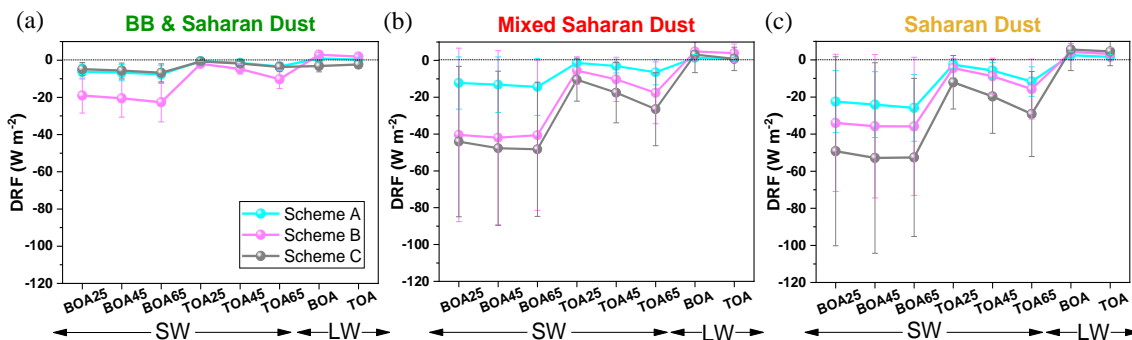
Figure 9: Mean values of SW and LW DRF at BOA and TOA and along with their SD for the three Schemes applied regarding the mixing state, namely a) BB & Saharan dust, b) Mixed Saharan dust and c) Saharan Dust. The dotted line represents the DRF zero value.

Finally, our interest is focused on the vertical DRF profiles from the surface (a.s.l.) up to 10 km height in the free troposphere, where airborne dust is usually found, as estimated by Scheme C at 45° SZA per station. The DRF profiles, in the SW region, presented in Figs. 10 (a-d), follow the aerosol extinction vertical structure. The DRF values at the BOA are high in absolute values with a cooling behavior and decreases with increasing height, while the magnitude is proportional to the aerosol load in the whole atmospheric column. Specifically, the DRF ranges from -150.0 to -1.9 W m^{-2} for Granada, from -38.1 to -3.7 W m^{-2} for Potenza, from -64.8 to -13.2 W m^{-2} for Athens and from -90.3 to -28.4 W m^{-2} for Limassol. The corresponding ranges of α_{532} are 0.286–0.029 km^{-1}, 0.268–0.088 km^{-1}, 0.135–0.078 km^{-1} and 0.547–0.214 km^{-1}, respectively. Peaks in α_{532} are observed usually between 2 and 6 km a.s.l. indicating the intrusion of dust that corresponds to a decrease in the solar radiation reaching the surface.
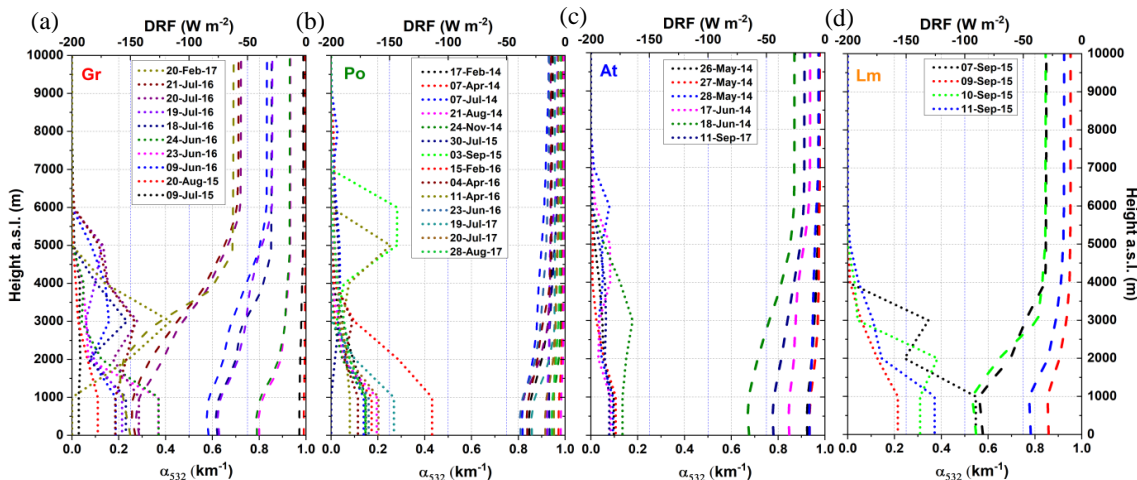
Figure 10: Vertical profiles of α_{532} (dotted lines) calculated from Raman lidar measurements along with the SW DRF (dashed lines) estimated from Libradtran simulations for the sites of: a) Granada, b) Potenza, c) Athens and d) Limassol, at 45° SZA.

5. Conclusions

The characteristics of the dust aerosol optical, geometrical, and radiative properties over the Mediterranean region, were presented at this study. A total of 51 independent aerosol lidar measurements of Saharan dust events
530   studied over 4 southern European cities were carefully selected and analyzed. The dust layers were usually observed between ~1.6 and ~5 km with δ_{p532} and LR_{532} values ranging from 0.16 to 0.35 and from 35 to 73 sr respectively, depending on the air mass mixing state. Significantly high AOT$_{532}$ values (0.40 ± 0.31) were found for Granada indicating that the dust outbreaks occurring over this area are more intense. Results of LR_{532} versus δ_{p532} are presented in order to elucidate the difference of pure dust and dust mixtures cases. Layers with lower δ_{p532} ($0.17 \pm$
535   0.01), AOT$_{532}$ (0.03 ± 0.02) and thicknesses (786 ± 212 m) have shown high dust mixing ratio, while the properties of the least or no mixed dust layers (δ_{p532}=0.32±0.02, AOT$_{532}$=0.32±0.23 and thickness=3158±1605 m) are in a good agreement with literature findings for pure Saharan dust cases (Tesche et al., 2009; Papayannis et al., 2009; Ansmann et al., 2012; Mona et al., 2012; Groß et al., 2011; 2013). Lidar stand-alone microphysical retrievals of R$_{eff}$, RRI and IRI are also differentiated by the level of mixing.

540   Three Schemes have been implemented to evaluate the DRF during the selected dust outbreaks: the model mass concentrations by BSC-DREAM8b (Scheme A), the mass concentrations calculated from lidar measurements (Scheme B) and the lidar extinction profiles along with the mean AOT$_{532}$ values (Scheme C). The DRF variations are strong and result from significant changes in the lidar retrieved extensive optical properties (α_{532}, β_{532}, AOT$_{532}$) or model mass estimations from the BSC-DREAM8b. A mean underestimation 31% of dust mass by BSC-
545   DREAM8b is leading to a significantly lower SW DRF compared to results obtained from the implementation of lidar profiles in LibRadtran. Additional variations in the SW range are introduced due to the variations in the available solar radiation during day that depends on the SZA. However, variations of the latter are significantly lower compared to the former. The vertical structure of a layer that gives information about the base, the thickness and the intensity (AOT) of a dust event is critically important, while additional information of its mixing state can
550   be also significant in RF and net heating rate estimations.

Our findings show a much more pronounced DRF at the BOA compared to the one at the TOA due to the low altitude of the studied layers (usually 2-4 km). Taking this into account we report DRF values at the BOA ranging from -40 to -13 W m^{-2} at SZA 25º, from -43 to -14 W m^{-2} at SZA 45º and from -44 to -15 W m^{-2} at 65º. At the TOA, the corresponding ranges per SZA are -9.5 to -1.4 W m^{-2} (25º), -16 to -3.3 W m^{-2} (45º) and -24.3 to -6.9
555   W m^{-2} (65º). In the LW range these values range from +1.6 to +3.5 W m^{-2} for the BOA and from +0.8 to +2.6 W m^{-2} for the TOA where again, the values of the latter reveal less perturbation.

The dependence of DRF on the accuracy of the vertical aerosol mass concentrations can give a wide range of possible values, however, the implemented Schemes can contribute to the characterization of the aerosols' radiative forcing effects over the Mediterranean region, being one of the most sensitive regions to climate change
560   forcing. Our findings suggest that a further investigation of aerosols' mixing state is needed since, not only their optical but also their microphysical properties and radiative forcing can strongly vary, depending on the mixing types. We recommend that the synergistic usage of observations and modeling in the next generation state of the art dust cycle models for the DRF should be intensified. The systematic use of remote sensing profiling measurements to radiative transfer models is stressed in this study, creating an essential tool that will allow us to
565   quantify both the cooling at the surface and the heating within the atmosphere produced by different aerosol types such as dust and its mixtures on a regional and a global scale.

Acknowledgements

O. S.'s research project has been financed through a scholarship from the General Secretariat for Research and Technology (GSRT) and the Hellenic Foundation for Research and Innovation (HFRI). The EARLINET lidar
570   data, were made available through the financial support by the ACTRIS Research Infrastructure Project funded by

10.5194/acp-2020-611
2020-07-01
Atmospheric Chemistry and Physics
Author(s) 2020. CC BY 4.0 License.
en

fggg

fff

gg

436, 1956.

Emde, C., Buras-Schnell, R., Kylling, A., Mayer, B., Gasteiger, J., Hamann, U., Kylling, J., Richter, B., Pause, C., Dowling, T. and Bugliaro, L.: The libRadtran software package for radiative transfer calculations (version 2.0.1), Geosci. Model Dev., 9(5), 1647–1672, doi:10.5194/gmd-9-1647-2016, 2016.

Fernández, A. J., Sicard, M., Costa, M. J., Guerrero-Rascado, J. L., Gómez-Amo, J. L., Molero, F., Barragán, R., Basart, S., Bortoli, D., Bedoya-Velásquez, A. E., Utrillas, M. P., Salvador, P., Granados-Muñoz, M. J., Potes, M., Ortiz-Amezcua, P., Martínez-Lozano, J. A., Artíñano, B., Muñoz-Porcar, C., Salgado, R., Román, R., Rocadenbosch, F., Salgueiro, V., Benavent-Oltra, J. A., Rodríguez-Gómez, A., Alados-Arboledas, L., Comerón, A. and Pujadas, M.: Extreme, wintertime Saharan dust intrusion in the Iberian Peninsula: Lidar monitoring and evaluation of dust forecast models during the February 2017 event, Atmos. Res., 228(June), 223–241, doi:10.1016/j.atmosres.2019.06.007, 2019.

Flaounas, E., Kotroni, V., Lagouvardos, K., Kazadzis, S., Gkikas, A. and Hatzianastassiou, N.: Cyclone contribution to dust transport over the Mediterranean region, Atmos. Sci. Lett., 16(4), 473–478, doi:10.1002/asl.584, 2015.

Freudenthaler, V., Esselborn, M., Wiegner, M., Heese, B., Tesche, M., Ansmann, A., Müller, D., Althausen, D., Wirth, M., Fix, A., Ehret, G., Knippertz, P., Toledano, C., Gasteiger, J., Garhammer, M. and Seefeldner, M.: Depolarization ratio profiling at several wavelengths in pure Saharan dust during SAMUM 2006, Tellus, Ser. B Chem. Phys. Meteorol., doi:10.1111/j.1600-0889.2008.00396.x, 2009.

Gkikas, A., Obiso, V., García-pando, C. P., Jorba, O. and Hatzianastassiou, N.: Direct radiative effects during intense Mediterranean desert dust outbreaks, , 8757–8787, 2018.

Gobbi, G. P., Barnaba, F., Giorgi, R. and Santacasa, A.: Altitude-resolved properties of a Saharan dust event over the Mediterranean, Atmos. Environ., 34, 5119–5127, 2000.

Groß, S., Tesche, M., Freudenthaler, V., Toledano, C., Wiegner, M., Ansmann, A., Althausen, D. and Seefeldner, M.: Characterization of Saharan dust, marine aerosols and mixtures of biomass-burning aerosols and dust by means of multi-wavelength depolarization and Raman lidar measurements during SAMUM 2, Tellus, Ser. B Chem. Phys. Meteorol., 63(4), 706–724, doi:10.1111/j.1600-0889.2011.00556.x, 2011.

Groß S., Esselborn M., Weinzierl B. , Wirth M.,Fix A., and P. A.: Aerosol classification by airborne high spectral resolution lidar observations, , 2487–2505, doi:10.5194/acp-13-2487-2013, 2013.

Groß, S., Freudenthaler, V., Ansmann, A., Baars, H., Haarig, M., Philipp, A., Seibert, P., Toledano, C., Weinzierl, B.: Ground-based polarization sensitive Raman lidar measurements of dust and pollution in the Eastern Mediterranean during the A-LIFE field experiment, in Geophysical Research Abstracts, p. 1., 2019.

Guerrero-Rascado, J. L., Ruiz, B. and Alados-Arboledas, L.: Multi-spectral Lidar characterization of the vertical structure of Saharan dust aerosol over southern Spain, Atmos. Environ., 42(11), 2668–2681, doi:10.1016/j.atmosenv.2007.12.062, 2008.

Guerrero-Rascado, J. L., Olmo, F. J., Avilés-Rodríguez, I., Navas-Guzmán, F., Pérez-Ramírez, D., Lyamani, H. and Arboledas, L. A.: Extreme saharan dust event over the southern iberian peninsula in september 2007: Active and passive remote sensing from surface and satellite, Atmos. Chem. Phys., 9(21), 8453–8469, doi:10.5194/acp-9-8453-2009, 2009.

Haapanala, P., Räisänen, P., Kahnert, M. and Nousiainen, T.: Sensitivity of the shortwave radiative effect of dust on particle shape: Comparison of spheres and spheroids, J. Geophys. Res. Atmos., 117(8), 1–12, doi:10.1029/2011JD017216, 2012.

Intergovernmental Panel on Climate Change: Synthesis Report. Contribution of Working Groups I, II and III to the Fifth Assessment Report of the Intergovernmental Panel on Climate Change, IPCC, Geneva, Switzerland., 2014.

ISO: Solar energy—Specification and classification of instruments for measuring hemispherical solar and direct solar radiation, Int. Organ. Stand., (9060), 11, 1990.

Jiménez-Guerrero, P., Pérez, C., Jorba, O. and Baldasano, J. M.: Contribution of Saharan dust in an integrated air quality system and its on-line assessment, Geophys. Res. Lett., 35(3), 1–6, doi:10.1029/2007GL031580, 2008.

Kim, M. H., Kim, S. W. and Omar, A. H.: Dust lidar ratios retrieved from the CALIOP measurements using the MODIS AOD as a constraint, Remote Sens., 12(2), doi:10.3390/rs12020251, 2020.

660   Kipp & Zonen: Instruction Manual CM121 Shadow ring., 2004.

Koepke, P., Gasteiger, J. and Hess, M.: Technical Note: Optical properties of desert aerosol with non-spherical mineral particles: Data incorporated to OPAC, Atmos. Chem. Phys., 15(10), 5947–5956, doi:10.5194/acp-15-5947-2015, 2015.

Kokkalis, P., Papayannis, A., Mamouri, R. E., Tsaknakis, G. and Amiridis, V.: The EOLE lidar system of the
665   National Technical University of Athens, 26th International Laser Radar Conference, June 25-29, 2012, Porto Heli, Greece., 2012.

Kokkalis, P., Jassar, H. K. Al, Solomos, S., Raptis, P., Hendi, H. Al, Amiridis, V., Papayannis, A., Sarraf, H. Al and Dimashki, M. Al: Long-Term Ground-Based Measurements of Aerosol Optical Depth over Kuwait City, Remote sens., 10(11), 18, doi:10.3390/rs10111807, 2018.

670   Kosmopoulos, P. G., Kazadzis, S., Taylor, M., Raptis, P. I., Keramitsoglou, I., Kiranoudis, C. and Bais, A. F.: Assessment of surface solar irradiance derived from real-time modelling techniques and verification with ground-based measurements, Atmos. Meas. Tech., 11(2), 907–924, doi:10.5194/amt-11-907-2018, 2018.

Madonna F., Amodeo A., Boselli A., Cornacchia C., Cuomo V., D'Amico G., Giunta A., Mona L., and P. G.: CIAO: The CNR-IMAA advanced observatory for atmospheric research, Atmos. Meas. Tech., 4(6), 1191–1208,
675   doi:10.5194/amt-4-1191-2011, 2011.

Mamouri, R. E., Ansmann, A., Nisantzi, A., Kokkalis, P., Schwarz, A. and Hadjimitsis, D.: Low Arabian dust extinction-to-backscatter ratio, Geophys. Res. Lett., 40(17), 4762–4766, doi:10.1002/grl.50898, 2013.

Mattis, I., Ansmann, A., Müller, D., Wandinger, U. and Althausen, D.: Dual-wavelength Raman lidar observations of the extinction-to-backscatter ratio of Saharan dust, Geophys. Res. Lett., doi:10.1029/2002gl014721, 2002.

680   Mayer, B., Kylling, A., Emde, C., Buras, R., Hamann, U., Gasteiger, J. and Richter, B.: libRadtran User's Guide, Ed. Libr. version 2.0.2, 1–155, 2017.

Meloni, D., Junkermann, W., di Sarra, A., Cacciani, M. De Silvestri, L., Di Iorio, T. Estellés, V., Gómez-Amo, J. L., Pace, G. and Sferlazzo, D. M.: Journal of Geophysical Research: Biogeosciences, J. Geophys. Res. Biogeosciences, 120(3), 693–706, doi:doi:10.1002/ 2014JG002832, 2015.

685   Meloni, D., di Sarra, A., DeLuisi, J., Di Iorio, T., Fiocco, G., Junkermann, W. and Pace, G.: Tropospheric aerosols in the Mediterranean: 2. Radiative effects through model simulations and measurements, J. Geophys. Res. D Atmos., 108(10), 1–16, doi:10.1029/2002jd002807, 2003.

Meloni, D., Di Sarra, A., Brogniez, G., Denjean, C., De Silvestri, L., Di Iorio, T., Formenti, P., Gómez-Amo, J. L., Gröbner, J., Kouremeti, N., Liuzzi, G., Mallet, M., Pace, G. and Sferlazzo, D. M.: Determining the infrared radiative
690   effects of Saharan dust: A radiative transfer modelling study based on vertically resolved measurements at Lampedusa, Atmos. Chem. Phys., 18(6), 4377–4401, doi:10.5194/acp-18-4377-2018, 2018.

Michaelides, S., Karacostas, T., Sánchez, J. L., Retalis, A., Pytharoulis, I., Homar, V., Romero, R., Zanis, P., Giannakopoulos, C., Bühl, J., Ansmann, A., Merino, A., Melcón, P., Lagouvardos, K., Kotroni, V., Bruggeman, A., López-Moreno, J. I., Berthet, C., Katragkou, E., Tymvios, F., Hadjimitsis, D. G., Mamouri, R. E. and Nisantzi, A.:
695   Reviews and perspectives of high impact atmospheric processes in the Mediterranean, Atmos. Res., 208(November 2017), 4–44, doi:10.1016/j.atmosres.2017.11.022, 2018.

Mishra, A. K., Klingmueller, K., Fredj, E., Lelieveld, J., Rudich, Y. and Koren, I.: Radiative signature of absorbing aerosol over the eastern Mediterranean basin, Atmos. Chem. Phys., 14(14), 7213–7231, doi:10.5194/acp-14-7213-2014, 2014.

700   Mona, L., Papagiannopoulos, N., Basart, S., Baldasano, J., Binietoglou, I., Cornacchia, C. and Pappalardo, G.: EARLINET dust observations vs . BSC-DREAM8b modeled profiles : 12-year-long systematic comparison at Potenza , Italy, , 8781–8793, doi:10.5194/acp-14-8781-2014, 2014.

Mona, L., Amodeo, A., Pandolfi, M. and Pappalardo, G.: Saharan dust intrusions in the Mediterranean area: Three years of Raman lidar measurements, J. Geophys. Res. Atmos., 111(16), 1–13, doi:10.1029/2005JD006569, 2006.

705   Mona, L., Liu, Z., Müller, D., Omar, A., Papayannis, A., Pappalardo, G., Sugimoto, N. and Vaughan, M.: Lidar measurements for desert dust characterization: An overview, Adv. Meteorol., 2012, doi:10.1155/2012/356265, 2012.

Müller, D., Ansmann, A., Mattis, I., Tesche, M., Wandinger, U., Althausen, D. and Pisani, G.: Aerosol-type-dependent lidar ratios observed with Raman lidar, J. Geophys. Res. Atmos., 112(D16202),
710   doi:10.1029/2006JD008292, 2007.

Navas-Guzmán, F., Bravo-Aranda, J. A., Guerrero-Rascado, J. L., Granados-Muñoz, M. J. and Alados-Arboledas, L.: Statistical analysis of aerosol optical properties retrieved by Raman lidar over Southeastern Spain, Tellus, Ser. B Chem. Phys. Meteorol., 65(1), doi:10.3402/tellusb.v65i0.21234, 2013.

Nisantzi, A., Mamouri, R. E., Ansmann, A., Schuster, G. L. and Hadjimitsis, D. G.: Middle East versus Saharan
715   dust extinction-to-backscatter ratios, , 7071–7084, doi:10.5194/acp-15-7071-2015, 2015.

Papadimas, C. D., Hatzianastassiou, N., Matsoukas, C., Kanakidou, M., Mihalopoulos, N. and Vardavas, I.: The direct effect of aerosols on solar radiation over the broader Mediterranean basin, Atmos. Chem. Phys., 12(15), 7165–7185, doi:10.5194/acp-12-7165-2012, 2012.

Papayannis, A., Mamouri, R. E., Amiridis, V. and Kazadzis, S.: Papayannis et al. - 2009 - Annales Geophysicae
720   Systematic lidar observations of Saharan dust layers over Athens , Greece in the frame of EARLINET project (2004 – 2006).pdf, , (2006), 3611–3620, 2009.

Pérez, C., Nickovic, S., Pejanovic, G., Baldasano, J. M. and Özsoy, E.: Interactive dust-radiation modeling: A step to improve weather forecasts, J. Geophys. Res. Atmos., 111(16), doi:10.1029/2005JD006717, 2006.

Petzold, A., Veira, A., Mund, S., Esselborn, M., Kiemle, C., Weinzierl, B., Hamburger, T., Ehret, G., Lieke, K. and
725   Kandler, K.: Mixing of mineral dust with urban pollution aerosol over Dakar (Senegal): Impact on dust physico-chemical and radiative properties, Tellus, Ser. B Chem. Phys. Meteorol., 63(4), 619–634, doi:10.1111/j.1600-0889.2011.00547.x, 2011.

Quijano, A. L., Sokolik, I. N. and Toon, O. B.: Radiative heating rates and direct radiative forcing by mineral dust in cloudy atmospheric conditions, J. Geophys. Res. Atmos., 105(D10), 12207–12219, doi:10.1029/2000JD900047,
730   2000.

Salvador, P., Alonso-Pérez, S., Pey, J., Artíñano, B., De Bustos, J. J., Alastuey, A. and Querol, X.: African dust outbreaks over the western Mediterranean Basin: 11-year characterization of atmospheric circulation patterns and dust source areas, Atmos. Chem. Phys., 14(13), 6759–6775, doi:10.5194/acp-14-6759-2014, 2014.

Samaras, S.: Microphysical retrieval of non-spherical aerosol particles using regularized inversion of multi-
735   wavelength lidar data. PhD Thesis, Institut für Mathematik, Numerische Mathematik - Inverse Probleme, University of Potsdam, Germany., 2016.

Shang, X., Xia, H., Dou, X., Shangguan, M., Li, M. and Wang, C.: Adaptive inversion algorithm for 1.5µm visibility lidar incorporating in situ Angstrom wavelength exponent, Opt. Commun., 418, 129–134, doi:10.1016/j.optcom.2018.03.009, 2018.

740   Sicard, M., Bertolín, S., Mallet, M., Dubuisson, P. and Comerón, A.: Estimation of mineral dust long-wave radiative forcing: Sensitivity study to particle properties and application to real cases in the region of Barcelona, Atmos. Chem. Phys., 14(17), 9213–9231, doi:10.5194/acp-14-9213-2014, 2014.

Solomos, S., Bougiatioti, A., Soupiona, O., Papayannis, A., Mylonaki, M. and Papanikolaou, C.: E ff ects of regional

and local atmospheric dynamics on the aerosol and CCN load over Athens, Atmos. Environ., 197(May 2018), 53–65, doi:10.1016/j.atmosenv.2018.10.025, 2019.

Soupiona, O., Papayannis, A., Kokkalis, P., Mylonaki, M., Tsaknakis, G., Argyrouli, A. and Vratolis, S.: Long-term systematic profiling of dust aerosol optical properties using the EOLE NTUA lidar system over Athens, Greece (2000–2016), Atmos. Environ., 183(April), 165–174, doi:10.1016/j.atmosenv.2018.04.011, 2018.

Soupiona, O., Samaras, S., Ortiz-Amezcua, P., Böckmann, C., Papayannis, A., Moreira, G. A., Benavent-Oltra, J. A., Guerrero-Rascado, J. L., Bedoya-Velásquez, A. E., Olmo, F. J., Román, R., Kokkalis, P., Mylonaki, M., Alados-Arboledas, L., Papanikolaou, C. A. and Foskinis, R.: Retrieval of optical and microphysical properties of transported Saharan dust over Athens and Granada based on multi-wavelength Raman lidar measurements: Study of the mixing processes, Atmos. Environ., 214(July), 116824, doi:10.1016/j.atmosenv.2019.116824, 2019.

Stein, A. F., Draxler, R. R., Rolph, G. D., Stunder, B. J. B., Cohen, M. D. and Ngan, F.: Noaa's hysplit atmospheric transport and dispersion modeling system, Bull. Am. Meteorol. Soc., 96(12), 2059–2077, doi:10.1175/BAMS-D-14-00110.1, 2015.

Tegen, I., Bierwirth, E., Heinold, B., Helmert, J. and Wendisch, M.: Effect of measured surface albedo on modeled Saharan dust solar radiative forcing, J. Geophys. Res. Atmos., 115(24), 1–15, doi:10.1029/2009JD013764, 2010.

Tesche, M., Ansmann, A., Müller, D., Althausen, D., Engelmann, R., Freudenthaler, V. and Groß, S.: Vertically resolved separation of dust and smoke over Cape Verde using multiwavelength Raman and polarization lidars during Saharan Mineral Dust Experiment 2008, J. Geophys. Res. Atmos., 114(D13), doi:10.1029/2009JD011862, 2009.

Tsekeri, A., Lopatin, A., Amiridis, V., Marinou, E., Igloffstein, J., Siomos, N., Solomos, S., Kokkalis, P., Engelmann, R., Baars, H., Gratsea, M., Raptis, P. I., Binietoglou, I., Mihalopoulos, N., Kalivitis, N., Kouvarakis, G., Bartsotas, N., Kallos, G., Basart, S., Schuettemeyer, D., Wandinger, U., Ansmann, A., Chaikovsky, A. P. and Dubovik, O.: GARRLiC and LIRIC: Strengths and limitations for the characterization of dust and marine particles along with their mixtures, Atmos. Meas. Tech., 10(12), 4995–5016, doi:10.5194/amt-10-4995-2017, 2017.

Veselovskii, I., Hu, Q., Goloub, P., Podvin, T., Korenskiy, M., Derimian, Y., Legrand, M. and Castellanos, P.: Variability in lidar-derived particle properties over West Africa due to changes in absorption : towards an understanding, Atmos. Chem. Phys, 20, 6563–6581, doi:https://doi.org/10.5194/acp-20-6563-2020, 2020.

World Meteorological Organization: Guide to meteorological instruments and methods of observation., WMO-No.8., 2018.